

Cerium-doped indium oxide transparent electrode for semi-transparent perovskite and perovskite/silicon tandem solar cells

Shichong An^{a,b}, Peirun Chen^{a,b}, Fuhua Hou^{a,b}, Qi Wang^{a,b}, Heng Pan^{a,b}, Xinliang Chen^{a,b}, Xiaonan Lu^{c,d}, Ying Zhao^{a,b}, Qian Huang^{a,b,*}, Xiaodan Zhang^{a,b}

^a Institute of Photo Electronic Thin Film Devices and Technology of Nankai University, Tianjin 300350, PR China

^b Photoelectronic Thin Film Devices and Technology of Tianjin, 300350, PR China

^c Food Nutrition and Health Program, The University of British Columbia, Vancouver V6T 1Z4, Canada

^d Department of Chemistry, The University of British Columbia, Vancouver V6T 1Z1, Canada

ARTICLE INFO

Keywords:

Transparent electrode
Room temperature
Mobility
Transmittance
Solar cells

ABSTRACT

Perovskite and perovskite/silicon tandem solar cells hold great promise for commercialization for their high efficiency and low cost. One of the major challenges for semi-transparent perovskite and tandem devices is the availability of suitable transparent electrodes. Here, we report an alternative high-performance cerium-doped indium oxide (ICO) transparent electrode with high mobility, low carrier concentration and high transmittance by Radio frequency (RF) magnetron sputtering at room temperature (RT) for thus applications. A high mobility of 51.6 cm²/Vs, a low resistivity of $5.74 \times 10^{-4} \Omega \text{ cm}$ as well as a high average transmittance of 83.5% ranging from 400 nm to 1800 nm were obtain at RT. The spectral response of a planar semi-transparent perovskite solar cell (ST-PSC) proportion accelerated in 450–700 nm range and resulted in an absolute 1.1 mA/cm² (from 17.38 to 18.48 mA/cm²) and 1.47 mA/cm² (from 13.63 to 15.10 mA/cm²) short-circuit current improvement by replacing commercial ITO electrodes with ICO at different illuminate sides. Finally, the preliminary perovskite/silicon-heterojunction (SHJ) two-terminal tandem solar cell achieves a relative 8.06% improvement in power conversion efficiency (*PCE*) (from 18.85% to 20.37%) in the use of ICO transparent electrode, illustrating a promising alternative transparent electrode to further improve high-efficiency semi-transparent perovskite and its tandem solar cells.

1. Introduction

Extensive research interest has focused on perovskite solar cells (PSCs) and its tandem devices due to its high efficiency, wide bandgap, and low fabrication cost (Green, 2016). Semi-transparent perovskite solar cells (ST-PSCs) are currently the focus of research studies due to their high power conversion efficiency (*PCE*) combined with crystalline silicon (c-Si) (Dewi et al., 2019; Hossain et al., 2019; Kim et al., 2019; Duong et al., 2017) or chalcogenide solar cells (Han et al., 2018; Bailie et al., 2015). Within the last two years, there have been several encouraging demonstrations of perovskite/silicon tandem devices with a *PCE* superior to that of their (high-performance) c-Si bottom-cells. Furthermore, the latest record *PCE* of a perovskite/silicon tandem has reached to a certified 28% (Oxford, 2019), thereby surpassing the best-in-class reported for single-junction c-Si (26.7%) (NREL, 2018). Parasitic absorption in transparent electrodes is one of the main challenges to enabling *PCEs* for perovskite-based tandem solar cells beyond 30%

(Jacobs et al., 2019). Additionally, in devices with soft materials such as perovskite, the high temperatures during deposition and post-annealing may accelerate methylammonium iodide evolution and result in irreversible damage of the perovskite active layer and the organic carrier extraction layers (Loper et al., 2015). Thus, one of the major challenges for ST-PSCs is the availability of suitable transparent electrode material in a low temperature procedure. Importantly, the transparent electrode is not only the first necessary development for a semi-transparent perovskite device, but also the missing building block for the integration in a monolithic device (Loper et al., 2015).

Ideally, transparent electrodes feature simultaneously a high lateral conductivity and broadband transparency to minimize resistive losses and to increase the performance throughout the solar spectrum on device level, respectively. Significant efforts have been made (Loper et al., 2015; You et al., 2015), and among them sputtered transparent conductive oxides (TCOs) can be regarded as the ideal candidates because of their high transmittance in the visible and near-infrared (NIR)

* Corresponding author.

E-mail address: carolinehq@nankai.edu.cn (Q. Huang).

<https://doi.org/10.1016/j.solener.2019.12.040>

Received 17 August 2019; Received in revised form 11 December 2019; Accepted 14 December 2019

Available online 21 December 2019

0038-092X/ © 2019 Published by Elsevier Ltd on behalf of International Solar Energy Society.

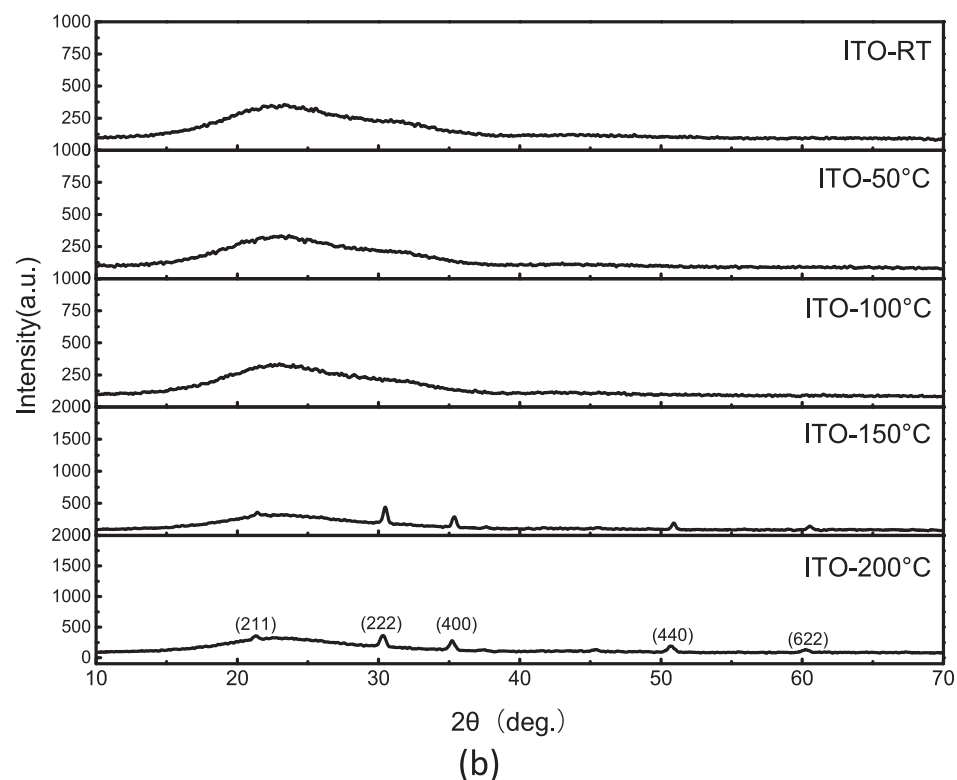
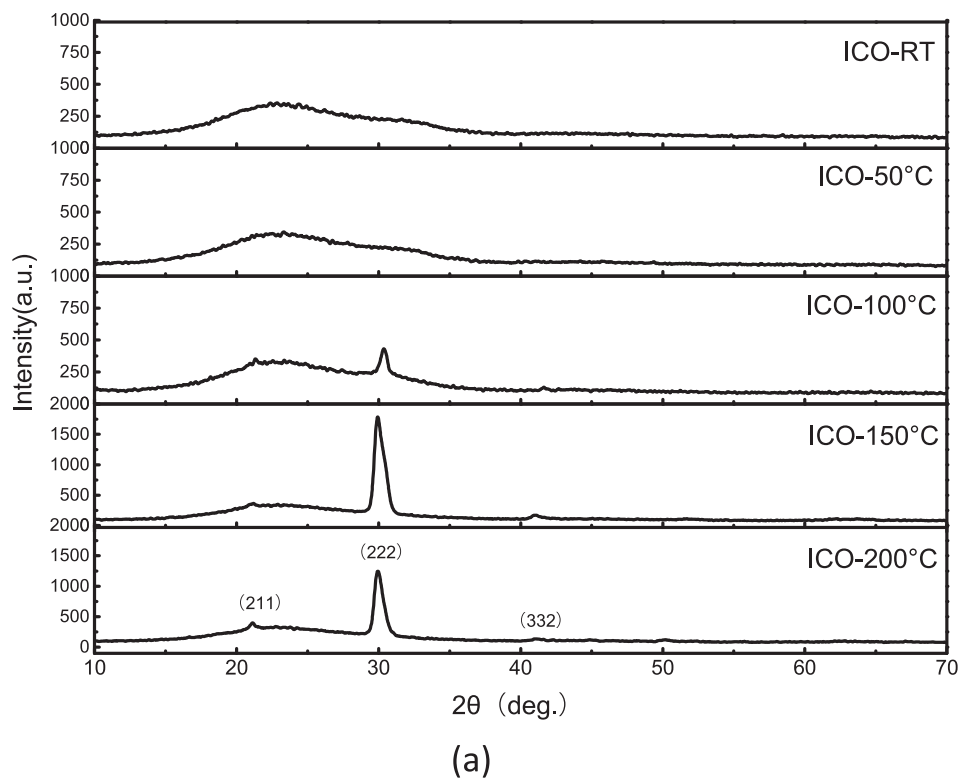


Fig. 1. (a) X-ray diffraction patterns of ICO and (b) ITO films.

region, low sheet resistance, good chemical stability and process reproducibility (Ellmer, 2012). To fulfill the seemingly contradictory transparency and conductivity requirement, strategies to increase the carrier mobility are required. It is critical that the transparent electrodes should combine a high conductivity with a minimal free-carrier absorption. Losses associated with the parasitic absorption caused by free-carrier can be reduced by decreasing the carrier density of the

transparent electrode (Koida et al., 2007). On the other hand, increase in the carrier mobility is required to maintain a high conductivity. Motivated by these criteria, some TCOs based on doped In_2O_3 have already been explored for tandem solar cells, such as ITO, Zr-doped In_2O_3 (IZRO) and ITO/H-doped In_2O_3 ($\text{In}_2\text{O}_3\text{:H}$) bilayer electrodes. In this, ITO, whereas being well established, is of limited appeal because of its low mobility and high parasitic absorption especially in the NIR

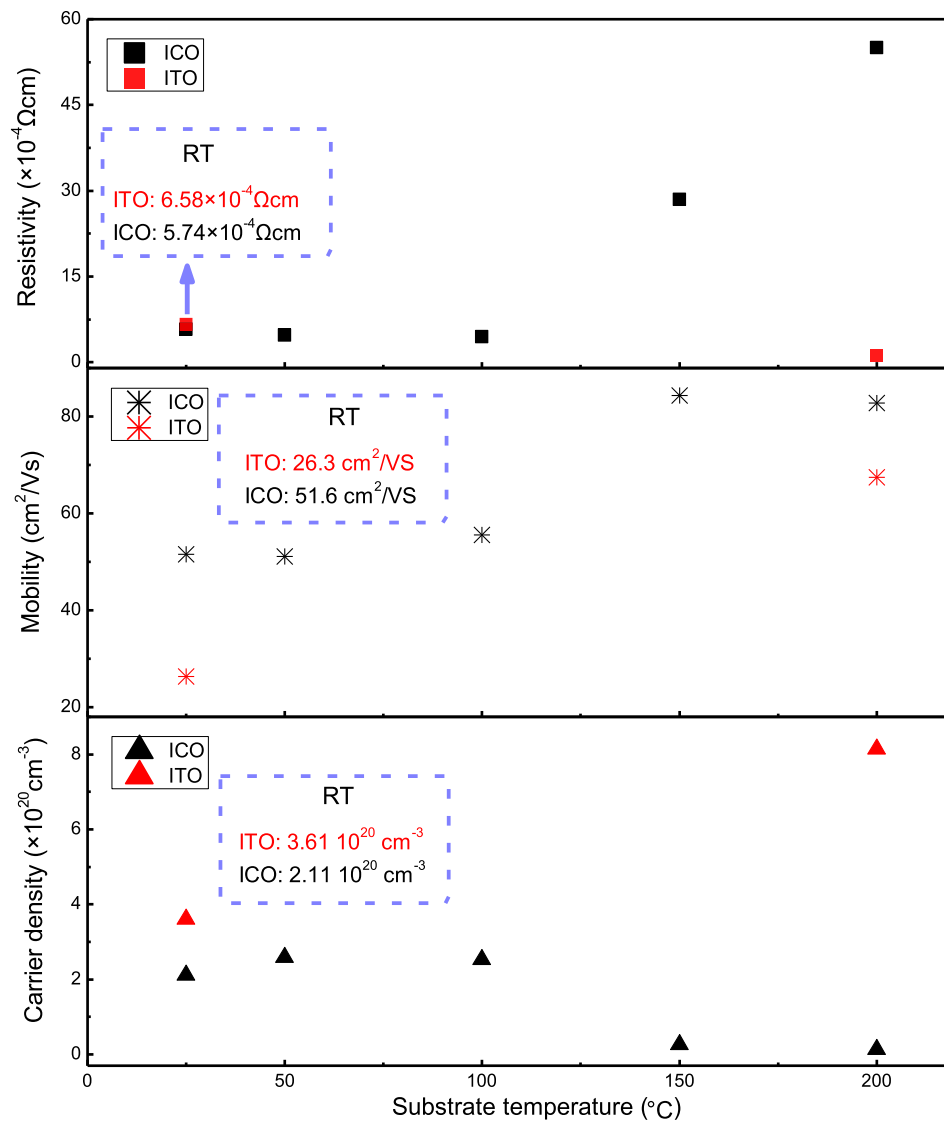


Fig. 2. Electrical properties of ICO and ITO films.

range (Morales-Masis et al., 2017), or it needs a post-annealing process (at 100 °C for 10–15 min) to enable its mobility $> 40 \text{ cm}^2/\text{Vs}$ (Ramos et al., 2018; Bush et al., 2017). IZRO has been explored as another promising TCO with a high mobility and NIR transparency, resulting in improved short circuit current density, compared to ITO in silicon heterojunction solar cells (Morales-Masis et al., 2018) and perovskite/silicon tandem device (Aydin et al., 2019). Unfortunately, this IZRO still has limitations because of its low mobility as-deposited and need a post-annealing process (at 200 °C for 25 min) (Aydin et al., 2019). Conversely, crystalline $\text{In}_2\text{O}_3:\text{H}$ has a very high mobility and optical transparency (Koida et al., 2007). However, this TCO may degrade the device performance due to water vapor effusion (Koida et al., 2009).

Recently, Ce-doped In_2O_3 (ICO) has been explored as a promising electrode with micro-strain in the vicinity to the dopant sites and density of oxygen vacancies could be reduced by CeO_2 doping. With these benefits, excellent optoelectronic properties such as high transparency, wide bandgap ($> 3.5 \text{ eV}$), and high conductivity, combined with high NIR transparency were obtained to improve crystallinity at 150 °C by DC arc-discharge ion-plating and post-annealing at 200 °C (Kobayashi et al., 2014; Eiji et al., 2016). Therefore, a procedure at room temperature (RT) makes it competitive for the application in perovskite and its tandem solar cells.

In this study, we thoroughly studied the structural and

optoelectronic properties of radio frequency (RF) sputtered ICO films, especially at room deposition temperature. Improvements of light transmittance in 300–1800 nm range and carrier mobility are detected in these films deposited at RT compared to a conventional ITO transparent electrode. Each promotion is tested in external quantum efficiency (EQE) and J - V detections. An initial PCE was then measured of more than 14% and 20% respectively to confirm its applicability for high-efficiency ST-PSCs and perovskite/SHJ two-terminal tandem solar cells. Thus, this high-quality ICO transparent electrode with improved full spectrum performance and carrier mobility at RT make it a promising electrode for perovskite single junction and perovskite-based tandem solar cells.

2. Experimental methods

ICO and ITO films about 100 nm ($\pm 5 \text{ nm}$) thick were deposited on Eagle XG glass substrates by RF magnetron sputtering in a KJLC Lab-18 sputtering system. The source materials for TCO deposition in this study were a ceramic $\text{In}_2\text{O}_3:\text{CeO}_2$ target (3 wt%) and ceramic $\text{In}_2\text{O}_3:\text{SnO}_2$ target (10 wt%), respectively. We maintained the sputtering chamber at a base pressure less than $1 \times 10^{-5} \text{ Pa}$ before each deposition. The distance between the substrate and target was maintained at 190 mm. We applied both low power density ($2.6 \text{ W}/\text{cm}^2$) and low pressure

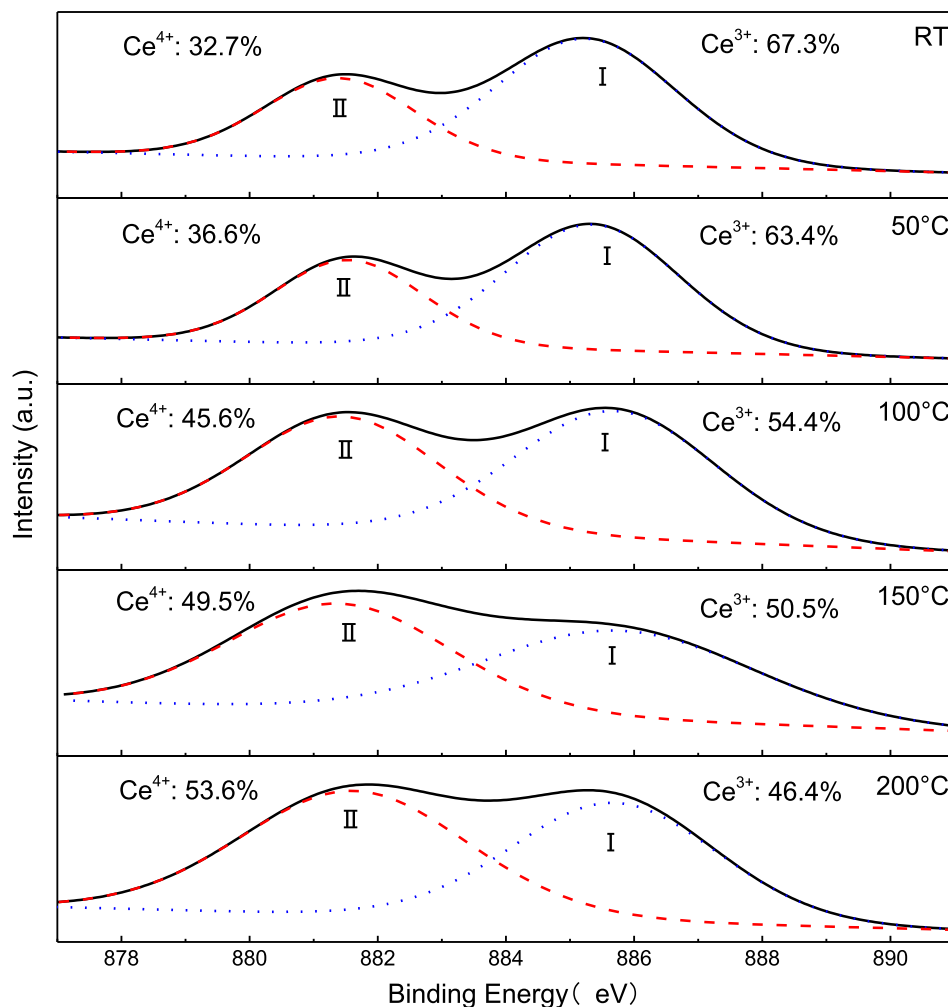


Fig. 3. XPS spectra of Ce 3d for ICO films.

(1.5 mTorr) along with pure Ar plasma condition. The substrate temperature varied from RT to 200 °C.

We applied the van der Pauw method (Qing et al., 2018) to determine sheet resistance, Hall mobility and carrier concentration at 22 °C in an HL5500 Hall System. Film thicknesses were measured by using a Dektak 3030 profilometer. The crystal orientation was determined by using X-ray diffraction (XRD) in an X'Pert PRO system. Moreover, we analyzed the bonding state of the films by using an Axis Ultra X-ray photoelectron spectrometer (XPS). The optical transmittance and reflection spectra of 200–1800 nm were collected by using a UV–Vis–NIR Varian-Cary 5000 spectrophotometer. The cross-section image was obtained by using a ThermoFisher Apreo SEM system.

ICO and ITO films were applied as the transparent electrode for ST-PSCs and perovskite/SHJ tandem solar cells, respectively. The structure of single junction ST-PSC is stacked as: ITO-coated glass with sheet resistance of about 10 Ω/sq; 40 nm SnO₂ hole-blocking layer; 400 nm FA_{0.75}MA_{0.25}PbI_{2.25}Br_{0.75} absorber layer; 150 nm Spiro-OMeTAD hole-transporting layer; 9 nm MoO_x buffer layer; 100 nm ICO (ITO) transparent electrode with shadow masked gold grid electrode. When transformed ITO substrate into c-Si bottom cell with modified tunnel junction, a monolithic perovskite/SHJ tandem device was obtained. The detailed preparation process has been reported in our previous works (Zhu et al., 2018; Zhu et al., 2018).

We measured *J*-*V* under 1-sun (AM 1.5, 25 °C, 100 mW/cm²) by using a Wacom WXs-156s-l2 dual-beam solar simulator. Simulation of AM1.5 spectrum was conducted through superpositioning the two filtered light sources of the simulator with calibration. The *EQE* curves

were carried out with our assembled system equipped with the dedicated illuminator, monochromator and lock-in amplifier. To get the *EQE* values in tandem device, monochromatic light sources (700 nm and 400 nm) were provided to bias the top or bottom part.

3. Results and discussion

We obtained XRD patterns of ICO and ITO films prepared at different substrate temperatures. As shown in Fig. 1(a), no peaks were observed for ICO films that were deposited below 100 °C. As the substrate temperature increased, the amorphous phase changed to polycrystalline structure, with the most prominent peak of (2 2 2) and weak planes of (2 1 1) and (3 3 2). The prominent (2 2 2) peak maximized intensity at 150 °C, whereas the (2 1 1) peak was inclined to a higher temperature. Additionally, the (2 2 2) peak position had a slight shift as the substrate temperature was increased, indicating variations of the residual stress in these films (Meng and Placido, 2003). Note that no peaks of Ce-oxides such as CeO₂ and Ce₂O₃ were observed, which implies that the cerium source replaces indium substitutionally. The average crystallite size for (2 2 2) peaks calculated by Scherrer's formulation (Bender and Douloufakis, 2001) increased initially and then decreased along with the increase in temperature, as the largest grain size of 17.5 nm occurs at 150 °C. For comparison, XRD patterns of ITO films were added in Fig. 1(b). The crystallite tendency bring into correspondence with ICO films. The (2 2 2) preferential orientation appeared at 150 °C, and the intensity significantly lower than ICO films which prepared at the same condition. As all the peak intensities were

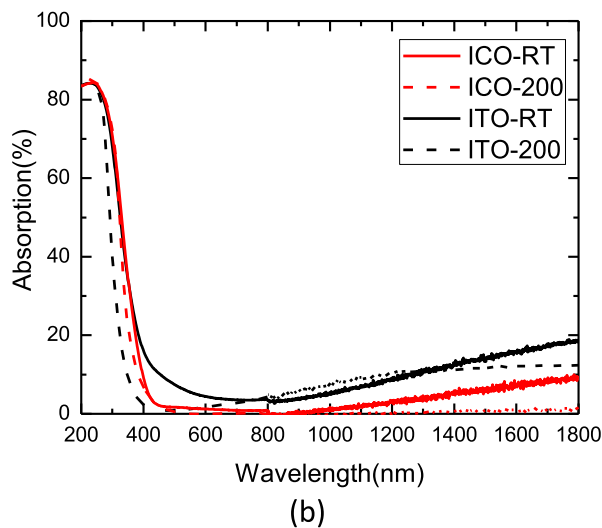
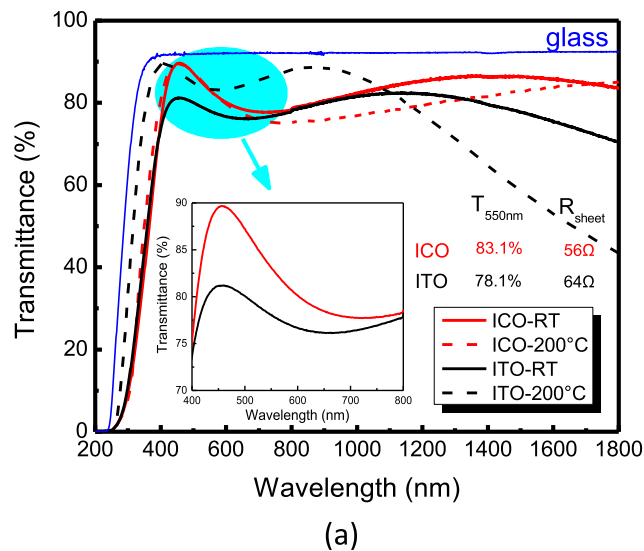


Fig. 4. (a) Transmittance and (b) absorption of ICO and ITO films deposited at RT and 200 °C.

normalized in common, these results indicate that the ICO layers had a relatively lower crystallization temperature, when compared to industrial ITO films with optimal crystallization temperature of over 200 °C in a magnetron sputtering procedure (Meng and Santos, 1998).

Fig. 2 summarizes the variations of the electrical properties of ICO films deposited at different substrate temperatures. In addition, the electrical properties of ITO films prepared at RT and 200 °C were also compared. The film resistivity (ρ) depends on the concentration (n) and mobility (μ) of relevant free carriers as follows: $\rho = (ne\mu)^{-1}$, where e is the electronic charge (Du et al., 2014). Low carrier concentration and high mobility were obtained for the ICO samples deposited at RT. As the carrier concentration decreased from 3.61×10^{20} to $2.11 \times 10^{20} \text{ cm}^{-3}$, the carrier mobility improved from 26.3 to $51.6 \text{ cm}^2/\text{Vs}$ compared to ITO films in our system.

Then we compared the binding characteristics of the atoms, which compose the ICO layers to be deposited at a variety of temperatures. The curve-fitted Ce 3d peaks for different samples are shown in Fig. 3. The Ce 3d peak for ICO film was resolved into two Gaussian-Lorentzian components. The high binding-energy peak of $885.4 \pm 0.2 \text{ eV}$ is associated with Ce^{3+} ions, which are surrounded by O (or substitutional In) atoms. This result validated the availability of Ce–O bonds in the ICO matrix. In comparison, the low binding-energy component at $881.6 \pm 0.2 \text{ eV}$ was due to the activated Ce^{4+} ions, which could offer

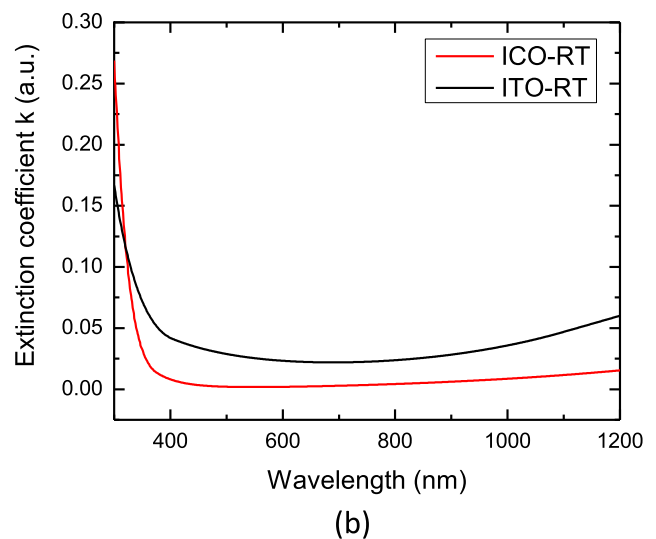
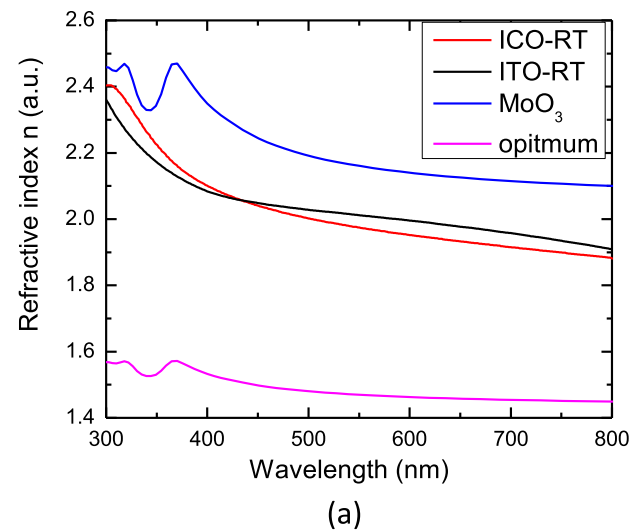


Fig. 5. (a) Calculated refractive index n and (b) extinction coefficient k of ICO and ITO thin films deposited at RT.

effective donors in the lattice (Watanabe et al., 2009; Bêche et al., 2010). In nominally n -type In_2O_3 , the dopant usually acts as substitutions or interstitials in the lattice. When the radius of dopant atom is approximately equal to that of In atom, the formation of substitution defect is lower as well as interstitial hydrogen could locate between O–In bonds. When Ce is doped, the Ce_{In} defect will form. If Ce atom could be fully oxidized to form a Ce^{4+} condition, a remaining free electron will be released into the lattice making the Ce_{In} act as a benefactor in In_2O_3 films (Paine et al., 1999). If Ce^{3+} ion was formed, no more free electron could be offered to increase the carrier concentration and electrical conductivity, but makes the lattice distortion. This occurrence implies that Ce_{In} is an efficient defect creator in In_2O_3 lattice and indirectly reduced the carrier mobility. Therefore, the relative concentrations of Ce^{4+} ($\text{Ce}^{4+} \text{ at.}\% / \text{Ce at.}\%$) and Ce^{3+} ($\text{Ce}^{3+} \text{ at.}\% / \text{Ce at.}\%$) were calculated according to the area of Ce 3d (I) and Ce 3d (II) peaks for ICO films deposited at different substrate temperatures. As shown in Fig. 4, the calculated atomic percentages of Ce related to the active donor (Ce^{4+}) was 32.7% at room-temperature deposition, indicating effective doping at that condition. When the substrate temperature increased, the relative atomic ratio of active Ce^{4+} and Ce_{In} increased proportionally. We attribute this decrease in carrier concentration to a reduction in doubly charged oxygen vacancies during the oxidation procedure at a relative high substrate temperature, written as $\text{V}_{\text{O}}^{\bullet\bullet}$ in Kröger–Vink notation, which provide as shallow

Table 1
Carrier concentration and bandgap of different samples.

Samples	ICO-RT	ICO-200	ITO-RT	ITO-200
Carrier concentration	$2.11 \times 10^{20} \text{ cm}^{-3}$	$1.37 \times 10^{19} \text{ cm}^{-3}$	$3.61 \times 10^{20} \text{ cm}^{-3}$	$8.14 \times 10^{20} \text{ cm}^{-3}$
Optical bandgap	3.61 eV	3.61 eV	3.61 eV	3.66 eV

donors (Tan et al., 2017).

Fig. 2 also displays the temperature dependence of the Hall mobility of ICO films that are dominated by ionized impurity scattering and lattice scattering. The crystallization quality improves, so the lattice scattering-which due to optical and acoustical phonons and piezoelectric scattering and is independent of carrier density-was reduced along with the increase in temperature. On the other hand, the ionized impurity scattering decreases which depends on the V_O density decreases. On behalf of these two advantages, the maximum of the mobility reached to $84.3 \text{ cm}^2/\text{Vs}$ at 150°C . Additionally, the carrier mobility of this ICO transparent electrode surpass the recently reported ITO ($43 \text{ cm}^2/\text{Vs}$ with a 15 min post-annealing at 100°C (Bush et al., 2017) and IZRO (maximum at $32 \text{ cm}^2/\text{Vs}$ as-deposited and up to $77 \text{ cm}^2/\text{Vs}$ under a 25 min post-annealing at 200°C (Meng and Placido, 2003) in perovskite tandem solar cells.

Taken together, the lowest migration barriers for oxygen are obtained by diffusion employing the dumbbell and the rotated dumbbell interstitials, which highlights the importance of V_O in ICO films. In addition, the carrier concentration and mobility of ICO films is strongly dominated by the density of V_O . Moreover, sputtering-deposited ICO films could realize high mobility even when deposited at RT, without subsequent annealing. Finally, the ICO thin films deposited at RT achieved a resistivity enhancement of 12.8% (from $6.58 \times 10^{-4} \Omega \text{ cm}$ to $5.74 \times 10^{-4} \Omega \text{ cm}$) compared to the traditional ITO films.

Transmittance and conductivity are two important TCO parameters that can significantly affect the performance of transparent solar cell. High transparency and low absorption in the full spectrum can introduce high J_{sc} to tandem solar cell by reducing the absorption of parasitic light. As shown in Fig. 4a, the spectral transmittance was illustrated in a wide spectral range (200–1800 nm) and highlighted the difference in the short-wavelength range (400–800 nm) for different samples. The abbreviations of each sample are defined as ICO film deposited at RT (ICO-RT) and 200°C (ICO-200), ITO film deposited at RT (ITO-RT) and 200°C (ITO-200). The absorption spectra were calculated from the transmittance and reflection coefficients, as defined as: $A = 1 - (R + T)$, as illustrated in Fig. 4b. The absorption characteristics show that ICO films have lower parasitic absorption loss than ITO in visible and near-infrared range, regardless of deposition temperature. More specifically, we deduced the complex refractive index (n , k) of ICO and ITO films deposited at RT from the reflectance and transmittance measured at normal incidence, as shown in Fig. 5. Extended Cauchy mode has been applied from a theoretical point of view in consideration of the Kramers-Kronig relation (Li and Wu, 2004; Gao et al., 2011). A global optimization procedure has been employed to make the difference between calculated and measured optical characteristics to be minimum. The complex refractive index shows the advantages of ICO films in two aspects. First of all, wavelength-dependent refractive index (n) of ICO is lower than that of ITO in the range of 430–800 nm, which makes better optical matching between MoO_x ($n \sim 2.2$) and air ($n \sim 1$). The optical refractive index of MoO_x used in our structure was also deduced as shown in the blue curve in Fig. 4a, while the calculated optimal matching parameters are shown in purple. Secondly, extinction coefficient (k) possesses a distinct advantage over ITO in the whole wavelength range provides less parasitic absorption. Additionally, all of the samples have a collective absorption tail with high extinction coefficient (k) near the wavelength at 300 nm. The optical band gap of In_2O_3 films, with a direct transition, is determined by applying the Tauc model, and the Devis and Mott model in

the high absorbance region (Patil et al., 2011). In this work, the optical bandgaps extracted from the transmission spectra are 3.61 eV, 3.61 eV, 3.61 eV and 3.66 eV for ICO-RT, ICO-200, ITO-RT, and ITO-200, respectively.

In a heavily doped n-type semiconductor, the optical bandgap is a result of carrier concentration and dangling bond density at the forbidden band edge. In the doped In_2O_3 films, both band-gap renormalization and Burstein–Moss (BM) effect significantly contribute to the determination of blue shift of band gap. Modification of electronic states starts to appear in the crystal format, which is due to the fact that electron concentration is higher than the Mott critical value. The correlated motion of charge carriers and their scattering against ionized impurities leads to band-gap narrowing (BGN). Table 1 illustrates the carrier concentration and bandgap of different samples. The BM effect can be clearly observed as an absorption tail in the near-ultraviolet region appears as a blue-shift for the ITO-200 film with the highest carrier concentration. This phenomenon makes great coordination with the significant decline at the long wavelength range, which is related to the free-carrier absorption caused by surface plasmon polariton. In comparison, the optical band gaps of ICO-200 and ICO-RT samples show an equivalent value when the carrier concentration ranged from 1.37×10^{19} to $3.61 \times 10^{20} \text{ cm}^{-3}$. We attribute this result to the variation of dangling-bond density for different samples. The presence of dislocation, point defect, grain boundary and its strain state result in dangling bond of a semiconductor thin film. The negatively charged oxygen species in the current ICO films are absorbed onto the surface of the grain boundary, performing as the trapping site to generate the potential barriers. The removal of the defects, which act as non-radiative recombination centers, with the rise of temperature, affects the optical constants near the band gap and expands the optical band gap of ICO-200. Most importantly, the transmittance of ICO-RT over the whole visible and near-infrared region-especially in the 400–800 nm region-covers the absorption section of perovskite absorber layer. T_{550} and R_{sheet} values of both ICO and ITO films were specified in Fig. 4a. ICO film exhibits better optical and electrical performances than ITO film deposited at the same condition.

To summarize the transmittance results, we conclude that ICO transparent electrode deposited at RT provides a promising alternative to temperature-sensitive solar cells, such as perovskite or organic solar cells. About 5% average transmittance improvement was obtained on both perovskite sensitive range (from 400 nm to 800 nm, varied from 77.7% to 81.6% with glass substrate) and whole tandem configuration sensitive range (from 400 nm to 1800 nm, varied from 78.5% to 83.5%).

Finally, we emphasize the potentially improved conductivity and full-spectrum performance for transparent perovskite and tandem solar cells. Single-junction ST-PSC and perovskite/SHJ two-terminal tandem solar cells were co-deposited with the ICO or ICO transparent electrode both deposited at RT. The detailed ST-PSC structure is illustrated in Fig. 6a: 40-nm SnO_2 as hole-blocking layer; 400-nm $\text{FA}_{0.75}\text{MA}_{0.25}\text{PbI}_{2.25}\text{Br}_{0.75}$ as absorber layer; 150-nm Spiro-OMeTAD as hole transporting layer; 9-nm MoO_x as damage blocking layer; and 100-nm ICO or ITO as transparent electrode; 100 nm Au as grid electrode. Fig. 6b shows the cross-sectional SEM image of the fabricated ST-PSC with ICO transparent electrode (identified by the red rectangle inside). We conducted the J - V and EQE measurement so as to study the wavelength dependence and electrical performance of the targeted cells. The semi-transparent device with a top electrode area of $6 \text{ mm} \times 11 \text{ mm}$ is

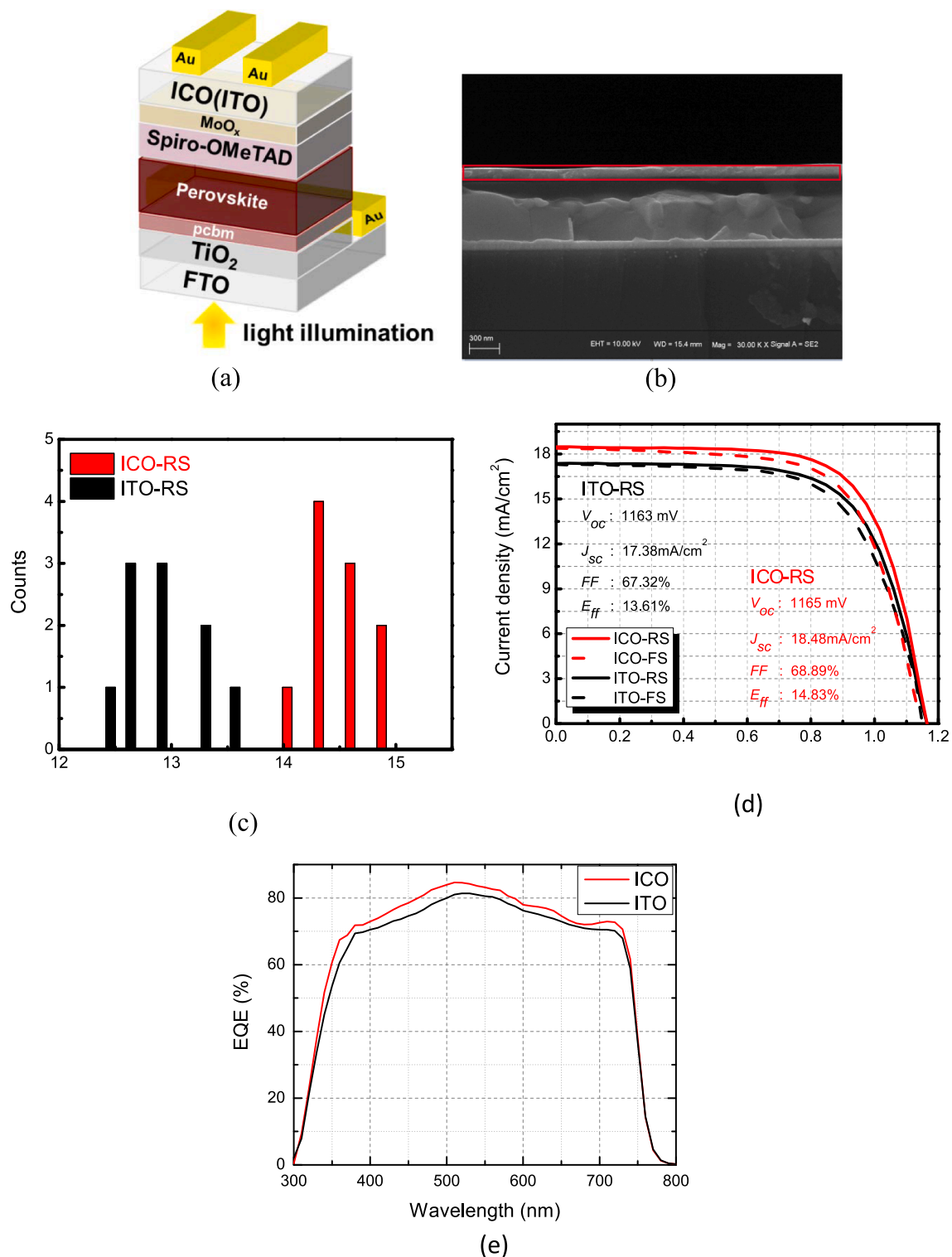


Fig. 6. (a) Device structure of ST-PSCs (b) device cross-section SEM image (the red rectangle inside shows the ICO transparent electrode) (c) PCE statistics of ST-PSCs with different transparent electrode (d) J-V curves of ST-PSCs with light illuminated from FTO side depending on scan direction and transparent electrode (ITO (black), ICO (red)), where solid and dash lines represent reverse scan (RS, from open-circuit to short-circuit) and forward scan (FS, from short-circuit to open-circuit), respectively (e) EQE curves of ST-PSCs with light illuminated from FTO side. (For interpretation of the references to color in this figure legend, the reader is referred to the web version of this article.)

illuminated through FTO side. Two groups of four cells were carried out with five test points for each cell. Samples in comparison in each group have the same trend of variation, with an average PCE of 12.97% or 14.44% using ITO or ICO as the transparent electrode, respectively. PCE statistics of the ICO- and ITO-based devices are shown in Fig. 6c. The

best performers with deviations less than 3% from the average value are shown in Fig. 6d as comparison. We scan the devices in a positive to negative voltage direction with a step size of 50 mV and a delay time between points of 0.2 s. Compared to the ITO-based device, the FF improved from 0.67 to 0.69 where the V_{oc} remained almost identical.

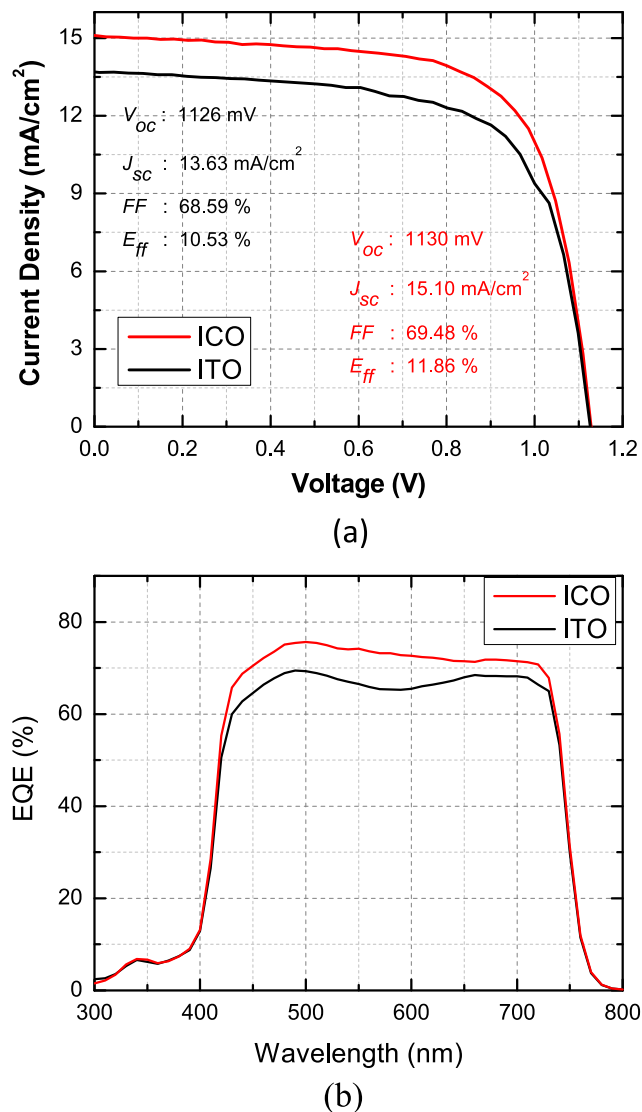


Fig. 7. (a) *J-V* and (b) *EQE* curves of ST-PSCs with light illuminated from ICO/ITO side.

This could be due to the reduction in ohmic losses at the TCO and TCO/p-contact. Hysteresis is shown in *J-V* curves of both ICO and ITO transparent electrode devices. Compared with ITO-based device, no significant difference in *J-V* curves between FS and RS is observed for ICO-based devices. *EQE* values shown in Fig. 6(e) were also improved in the whole wavelength range with ICO transparent electrode. And the integrated current density increase from 17.38 mA/cm² to 18.48 mA/cm² while leading a relative increment of 8.96% in *PCE* (from 13.61% to 14.83%).

With the need to be applied in perovskite/SHJ two-terminal tandem devices, light was then illustrated from the top ICO side. As shown in Fig. 7, the active-area (subtract the shielding area given by Au grid electrode) *PCE* and integrated current density decreased because of the parasitic absorption in Spiro-OMeTAD layer and the low reflectance at the FTO glass side. However, the influence caused by the optical characteristics of ICO transparent electrode is enhanced as the light just goes through it and then into the whole device. As shown in Fig. 7(b), the *EQE* values obtained an obviously average increment from 67.2% to 73.0% from 450 to 700 nm, where the average transmittance increases from 77.9% to 82.5% at the same wavelength range. We attribute this improvement to the complex refractive index advantage on both refractive index and extinction coefficient aspects. As a result, the

integrated current density increased from 13.63 mA/cm² to 15.10 mA/cm² for the single junction devices with the light illuminated from the ICO/ITO side. Furthermore, the ST-PSC with ICO transparent electrode possessed a high average transmittance of 67.21% at 800–1200 nm, where a good incident light window is provided for single crystal silicon bottom cells.

The structure of monolithic perovskite/SHJ tandem device was optimized in our laboratory condition as reported in our previous work (Zhu et al., 2018) and shown in Fig. 8a. The SHJ cells are comprised of intrinsic (i-type) a-Si and p-type a-Si layers deposited on the polished n-type c-Si (E_g = 1.1 eV) to form a p/n heterojunction on one side and a back surface field. The thickness of thermal evaporated ITO tunnel junction was set at 80 nm for equilibrium between protection of underlying layers and conductivity of electrode. Ultimately, we obtained monolithic perovskite/SHJ tandem solar cells with the *J-V* and *EQE* curves shown in Fig. 8b and c. Two groups of six cells were also carried out with two test points for each tandem solar cell. *PCE* statistics of the ICO- and ITO-based tandem devices are shown in Fig. 8b. Samples in comparison in each group have the same trend of variation, and the best performers in each group have deviations less than 5% from the average value are shown in Fig. 8c and d as comparison. The advantages of ICO in electrical and optical characteristics were well reflected in the cells performance. As a result, the maximal initial active-area *PCE* and integrated current density increased from 18.85% to 20.37% and 15.43 mA/cm² to 16.29 mA/cm², respectively, were achieved with ICO transparent electrode applying. The detailed parameters of solar cells with ICO an ITO transparent electrode were illustrated in Table 2.

The unsatisfactory result of *PCEs* is mainly resulted from the current loss induced by the unbalanced absorption between the perovskite top cell and the double-side-polished SHJ bottom cell and the parasitic absorption of Spiro-OMeTAD. The light absorption and transmittance could be further balanced by applying solvent engineering to optimize perovskite films in the tandem devices (Zhu et al., 2018). And we will further modify the rear textured SHJ bottom cell and alternatively hole transporting materials with high transmittance for further improvement in cells performance. The results illustrated in this paper demonstrate that the alternative high-performance ICO thin film with high mobility, low carrier concentration and high transmittance enables the fabrication of high-efficiency semi-transparent perovskite and tandem devices. These permit a further step towards the realization of high *PCE* tandem solar cells beyond the single-junction silicon cell limit. We will do our best to further exploit the ICO transparent electrode in tandem device applications.

4. Conclusion

In summary, using magnetron sputtering at RT, we achieved a high-performance ICO transparent electrode to effectively enhance the electricity and full-spectrum performance of the transparent electrode for high-efficiency ST-PSCs and perovskite/SHJ tandem solar cells. A high mobility of 51.6 cm²/Vs as well as a reduced resistivity of $5.74 \times 10^{-4} \Omega \text{ cm}$ were obtained at RT. The optical transmittance in the entire sensitive wavelength region was improved with an average transmittance boost of 5% compared to ITO films at the 400–1800 nm wavelength range, with more suitable refractive index and lower extinction coefficient. When applied in ST-PSCs and perovskite/SHJ two-terminal tandem solar cells, the advantages of ICO in electrical and optical characteristics were well reflected in the cells performance. Finally, we have successfully demonstrated the ST-PSC and perovskite/SHJ solar cell delivering a relative increment in *PCE* of 8.96% (from 13.61% to 14.83%) and 8.06% (from 18.85% to 20.37%), respectively, when comparing with conventional ITO transparent electrode. These results represent a further step to realize tandem cells transcending the silicon solar cell efficiency limitation.

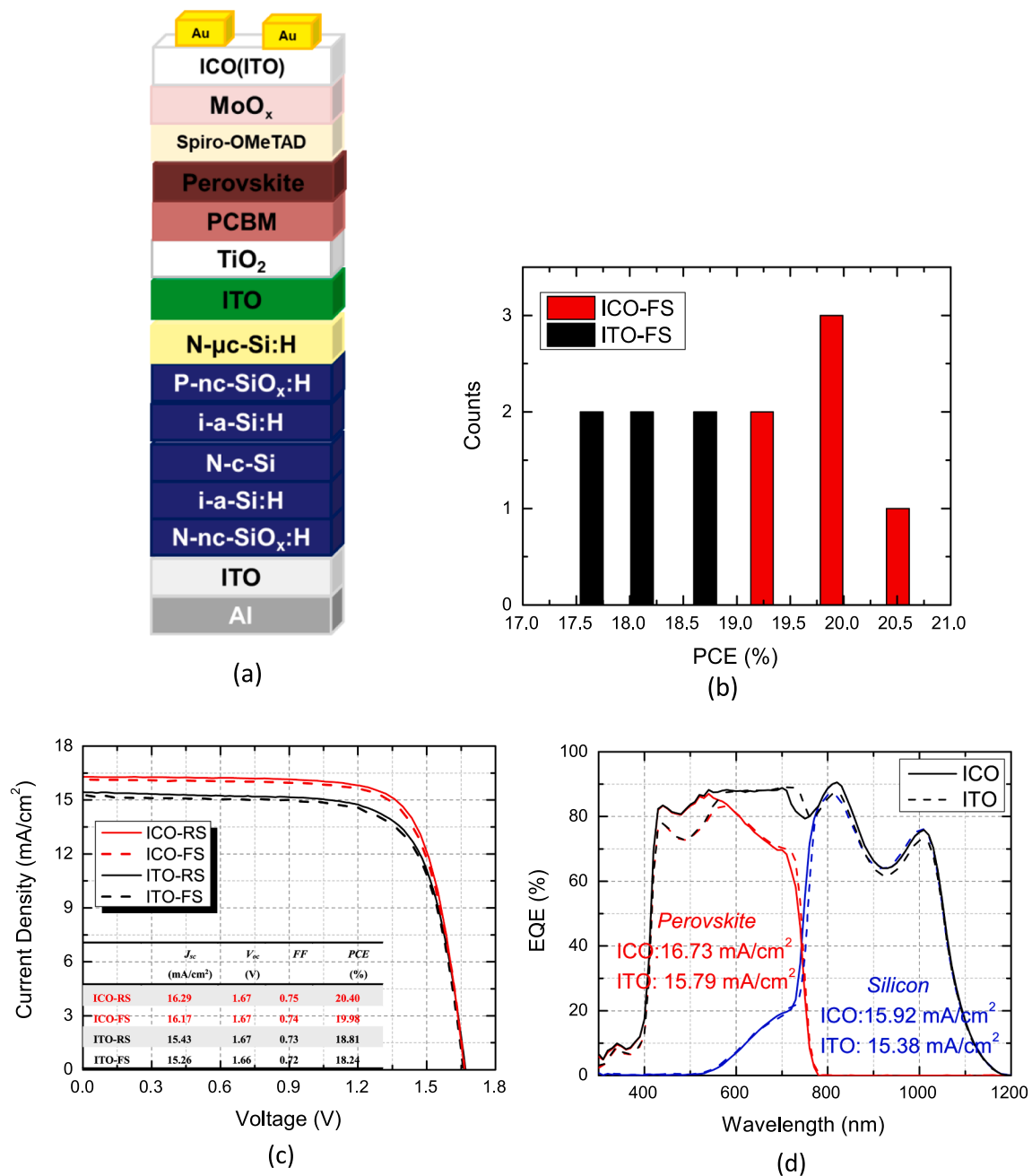


Fig. 8. (a) Device structure (b) PCE statistics of perovskite/SHJ tandem solar cells depending on different transparent electrode (ITO (black), ICO (red)) (c) J-V curves of perovskite/SHJ tandem solar cells depending on scan direction and transparent electrode (ITO (black), ICO (red)), where solid and dash lines represent reverse scan (RS, from open-circuit to short-circuit) and forward scan (FS, from short-circuit to open-circuit), respectively, and (d) EQE curves with red lines for perovskite top cells, blue lines for silicon top cells and black lines for tandem devices, while the solid and dash lines represent the behavior of ICO and ITO transparent electrodes respectively. (For interpretation of the references to color in this figure legend, the reader is referred to the web version of this article.)

Table 2
I-V characteristics of ST-PSCs and perovskite/SHJ tandem solar cells.

Structure	Front contract	J_{sc} (mA/cm ²)	V_{oc} (V)	FF (%)	PCE (%)
ST-PSC	ICO	18.48	1.17	68.89	14.83
ST-PSC	ITO	17.38	1.16	67.32	13.61
Tandem	ICO	16.29	1.67	74.86	20.37
Tandem	ITO	15.43	1.67	73.16	18.85

Declaration of Competing Interest

The authors declare that they have no known competing financial interests or personal relationships that could have appeared to influence the work reported in this paper.

Acknowledgment

This work was supported by the National Key Research Program of China (2018YFB1500104).

References:

- Aydin, E., De Bastiani, M., Yang, X.B., Sajjad, M., Aljamaan, F., Smirnov, Y., Hedhili, M.N., Liu, W.Z., Allen, T.G., Xu, L.J., Van Kerschaver, E., Morales-Masis, M., Schwingenschlogl, U., De Wolf, S., 2019. Zr-doped indium oxide (IZRO) transparent electrodes for perovskite-based tandem solar cells. *Adv. Funct. Mater.* 29, 1901741.
- Bailie, C.D., Christoforo, M.G., Mailoa, J.P., Bowring, A.R., Unger, E.L., Nguyen, W.H., Burschka, J., Pellet, N., Lee, J.Z., Gratzel, M., Noufi, R., Buonassisi, T., Salles, A., McGehee, M.D., 2015. Semi-transparent perovskite solar cells for tandems with silicon and CIGS. *Energ. Environ. Sci.* 8, 956–963.
- Bêche, E., Charvin, P., Perarnau, D., Abanades, S., Flamant, G., 2010. Ce 3d XPS investigation of cerium oxides and mixed cerium oxide ($\text{Ce}_x\text{Ti}_{1-x}\text{O}_2$). *Surf. Interface Anal.* 40, 264–267.
- Bender, M., Douloufakis, E., 2001. The influence of deposition parameters on room temperature ozone sensing properties of InO_x films. *Sens. Actuator B-Chem.* 80, 155–161.
- Bush, K.A., Palmstrom, A.F., Yu, Z.S.J., Boccard, M., Cheacharoen, R., Mailoa, J.P., McMeekin, D.P., Hoyer, R.L.Z., Bailie, C.D., Leijtens, T., Peters, I.M., Minichetti, M.C., Rolston, N., Prasanna, R., Sofia, S., Harwood, D., Ma, W., Moghadam, F., Snaith, H.J., Buonassisi, T., Holman, Z.C., Bent, S.F., McGehee, M.D., 2017. 23.6%-efficient monolithic perovskite/silicon tandem solar cells with improved stability. *Nat. Energy* 2 (4), 17009.
- Dewi, H.A., Wang, H., Li, J., Thway, M., Sridharan, R., Stangl, R., Lin, F., Aberle, A.G., Mathews, N., Bruno, A., Mhaisalkartie, S., 2019. Highly efficient semitransparent perovskite solar cells for four terminal perovskite-silicon tandems. *ACS Appl. Mater. Interfaces* 11 (37), 34178–34187.
- Du, J., Chen, X.L., Liu, C.C., Ni, J., Hou, G.F., Zhao, Y., Zhang, X.D., 2014. Highly transparent and conductive indium tin oxide thin films for solar cells grown by reactive thermal evaporation at low temperature. *Appl. Phys. A* 117, 815–822.
- Duong, T., Wu, Y.L., Shen, H.P., Peng, J., Fu, X., Jacobs, D., Wang, E.C., Kho, T.C., Fong, K.C., Stocks, M., Franklin, E., Blakers, A., Zin, N., McIntosh, K., Li, W., Cheng, Y.B., White, T.P., Weber, K., Catchpole, K., 2017. Rubidium Multication perovskite with optimized bandgap for perovskite-silicon tandem with over 26% efficiency. *Adv. Energy Mater.* 7, 1700228.
- Eiji, K., Yoshimi, W., Tetsuya, Y., Yoichi, Y., 2016. Cerium oxide and hydrogen co-doped indium oxide films for high-efficiency silicon heterojunction solar cells. *Sol. Energ. Mat. Sol. C.* 149, 75–80.
- Ellmer, K., 2012. Past achievements and future challenges in the development of optically transparent electrodes. *Nat. Photonics* 6, 809–817.
- Gao, L., Lemarchand, F., Lequime, M., 2011. Comparison of different dispersion models for single layer optical thin film index determination. *Thin Solid Films* 520 (1), 501–509.
- Green, M.A., 2016. Commercial progress and challenges for photovoltaics. *Nat. Energy* 1, 15015.
- Han, Q., Hsieh, Y.-T., Meng, L., Wu, J.-L., Sun, P., Yao, E.-P., Chang, S.-Y., Bae, S.-H., Kato, T., Bermudez, V., 2018. High-performance perovskite/ $\text{Cu}(\text{In}, \text{Ga})\text{Se}_2$ monolithic tandem solar cells. *Science* 361, 904–908.
- Hossain, M.I., Qarony, W., Ma, S.N., Zeng, L.H., Knipp, D., Tsang, Y.H., 2019. Perovskite/silicon tandem solar cells: from detailed balance limit calculations to photon management. *Nano-Micro Lett.* 11 (1), 58.
- Jacobs, D.A., Langenhorn, M., Sahli, F., Richards, B.S., White, T.P., Ballif, C., Catchpole, K.R., Paetzold, U.W., 2019. Light management: a key concept in high-efficiency perovskite/silicon tandem photovoltaics. *J. Phys. Chem. Lett.* 10 (11), 3159–3170.
- Kim, C.U., Yu, J.C., Jung, E.D., Choi, I.Y., Park, W., Lee, H., Kim, I., Lee, D.K., Hong, K.K., Song, M.H., Choi, K.J., 2019. Optimization of device design for low cost and high efficiency planar monolithic perovskite/silicon tandem solar cells. *Nat. Energy* 60, 213–221.
- Kobayashi, E., Watabe, Y., Yamamoto, T., 2014. High-mobility transparent conductive thin films of cerium-doped hydrogenated indium oxide. *Appl. Phys. Express.* 8, 015505.
- Koida, T., Fujiwara, H., Kondo, M., 2007. Hydrogen-doped In_2O_3 as high-mobility transparent conductive oxide. *J. Appl. Phys.* 46, 25–28.
- Koida, T., Fujiwara, H., Kondo, M., 2007. Hydrogen-doped In_2O_3 as high-mobility transparent conductive oxide. *Jpn. J. Appl. Phys.* 46, L685.
- Koida, T., Fujiwara, H., Kondo, M., 2009. High-mobility hydrogen-doped In_2O_3 transparent conductive oxide for a-Si: H/c-Si heterojunction solar cells. *Sol. Energy Mater. Sol. Cells* 93, 851–854.
- Li, J., Wu, S.-T., 2004. Extended Cauchy equations for the refractive indices of liquid crystals. *J. Appl. Phys.* 95 (3), 896–901.
- Loper, P., Moon, S.J., de Nicolas, S.M., Niesen, B., Ledinsky, M., Nicolay, S., Bailat, J., Yum, J.H., DeWolf, S., Ballif, C., 2015. Organic-Inorganic halide perovskite/crystalline silicon four-terminal tandem solar cells. *Phys. Chem. Chem. Phys.* 17, 1619–1629.
- Meng, L.J., Placido, F., 2003. Annealing effect on ITO thin films prepared by microwave-enhanced Dc reactive magnetron sputtering for telecommunication applications. *Surf. Coat. Tech.* 166, 44–50.
- Meng, L.J., Santos, M.P.D., 1998. Properties of indium tin oxide films prepared by reactive magnetron sputtering at different substrate temperature. *Thin Solid Films* 322, 56–62.
- Morales-Masis, M., De Wolf, S., Woods-Robinson, R., Ager, J.W., Ballif, C., 2017. Transparent electrodes for efficient optoelectronics. *Adv. Electron. Mater.* 3, 1600529.
- Morales-Masis, M., Rucavado, E., Monnard, R., Barraud, L., Holovsky, J., Despeisse, M., Boccard, M., Ballif, C., 2018. Highly conductive and broadband transparent Zr-doped In_2O_3 as front electrode for solar cells. *IEEE J. Photovoltaics* 8, 1202.
- NREL, 2018. Best Research-Cell Efficiencies. <https://www.nrel.gov/pv/cell-efficiency.html> (accessed Nov 30, 2018).
- Oxford PV perovskite solar cell achieves 28% efficiency, 2019. <https://www.oxfordpv.com/news/oxford-pv-perovskite-solar-cell-achieves-28-efficiency> (accessed Mar 8, 2019).
- Paine, D.C., Whitson, T., Janic, D., Beresford, R., Yang, C.O., Lewis, B., 1999. A study of low temperature crystallization of amorphous thin film indium–tin–oxide. *J. Appl. Phys.* 85, 8445–8450.
- Patil, V., Pawar, S., Chougule, M., Godse, P., Sakhare, R., Sen, S., Joshi, P., 2011. Effect of annealing on structural, morphological, electrical and optical studies of nickel oxide. *Thin Films. Adv. Technol.* 1, 35–41.
- Qing, F.Z., Shu, Y., Qing, L.S., Niu, Y.T., Guo, H., Zhang, S.Y., Liu, C.L., Shen, C.Q., Zhang, W.L., Mao, S.S., Zhu, W.J., Li, X.S., 2018. A general and simple method for evaluating the electrical transport performance of graphene by the van der Pauw–Hall measurement. *Sci. Bull.* 63 (22), 1521–1526.
- Ramos, F.J., Juttau, S., Posada, J., Bercegol, A., Rebai, A., Guillemot, T., Bodeux, R., Schneider, N., Loones, N., Ory, D., Broussillou, C., Goer, G., Lombez, L., Rousset, J., 2018. Highly efficient MoO_x -free semitransparent perovskite cell for 4T tandem application improving the efficiency of commercially-available Al-BSF silicon. *Sci. Rep.* 8, 16139.
- Tan, C.H., Tan, S.T., Lee, H.B., Ginting, R.T., Oleiwi, H.F., Yap, C.C., Jumali, M.H.H., Yahaya, M., 2017. Automated room temperature optical absorbance CO sensor based on In-doped ZnO nanorod. *Sens. Actuator B-Chem.* 248, 140–152.
- Watanabe, S., Ma, X., Song, C., 2009. Characterization of structural and surface properties of nanocrystalline TiO_2 – CeO_2 mixed oxides by XRD, XPS, TPR, and TPD. *J. Phys. Chem. C* 113, 14249–14257.
- You, P., Liu, Z., Tai, Q., Liu, S.H., Yan, F., 2015. Efficient semitransparent perovskite solar cells with graphene electrodes. *Adv. Mater.* 27, 3632–3638.
- Zhu, S., Hou, F., Huang, W., Yao, X., Shi, B., Ren, Q., Chen, J., Yan, L., An, S., Zhou, Z., Ren, H., Wei, C., Huang, Q., Li, Y., Hou, G., Chen, X., Ding, Y., Wang, G., Li, B., Zhao, Y., Zhang, X., 2018. Solvent engineering to balance light absorbance and transmittance in perovskite for tandem solar cells. *Solar RRL* 1800176c.
- Zhu, S., Yao, X., Ren, Q., Zheng, C., Li, S., Tong, Y., Shi, B., Guo, S., Fan, L., Ren, H., Wei, C., Li, B., Ding, Y., Huang, Q., Li, Y., Zhao, Y., Zhang, X., 2018. Transparent electrode for monolithic perovskite/silicon-heterojunction two-terminal tandem solar cells. *Nano Energy* 45, 280–286.

Further reading

- Agashe, C., Kluth, O., Hüpkens, J., Zastrow, U., Rech, B., Wuttig, M., 2004. Efforts to improve carrier mobility in radio frequency sputtered aluminum-doped zinc oxide films. *J. Appl. Phys.* 95 (4), 1911–1917.